OPEN ACCESS

Kashf Journal of Multidisciplinary Research
Vol: 03 - Issue 03 (2026)
P-ISSN: 3007-1992 E-ISSN: 3007-200X
https://kjmr.com.pk

NUMERICAL ANALYSIS OF AERODYNAMIC PERFORMANCE OF S-SERIES AEROFOILS FOR LOW-SPEED WIND TURBINE APPLICATIONS

Muhammad Punhal Sahto[1], Syed Nasir Mehdi Gardezi[2], Muhammad Hassan[3], Arfa[4], *Ali Nawaz Sanjrani[5], Maryam Khan[6], Hussain Gardezi[7], M. Waleed Sikandar[8]

[1, 2, 3, 4, 6, 7, 8]Mechanical Engineering Department NFC Institute of Engineering & Technology, Multan, Pakistan.

[5]Department of Mechanical Engineering, Mehran University of Engineering and Technology, MUET, SZAB Campus, Khairpur Mir's, Sindh, Pakistan.

Corresponding Author: (punhalsahto@nfciet.edu.pk, alinawaz.sanjrani@muetkhp.edu.pk)

DOI:(*https://doi.org/10.71146/kjmr871*)

Article Info

Abstract

Pakistan possesses a massive, untapped wind potential of over 346 GW along its coastal belt; however, average wind speeds remain moderate 5–7 m/s, leading to low efficiency in standard turbine designs. This study presents a comprehensive numerical evaluation of four S-series airfoils (S818, S825, S826, and S828) to identify the optimal geometry for these specific conditions. Using ANSYS Fluent for 2D analysis and ANSYS CFX for 3D cascade behavior, the airfoils were tested at angles of attack from -5° to 10° at flow velocities representing Pakistan's coastal profile. Results indicate that while S818 suffers from premature flow separation at low speeds, the S828 airfoil demonstrates superior aerodynamic efficiency and stall resistance. A multi-criteria decision matrix confirms S828 as the most suitable candidate 95% efficiency score for localized small-scale wind energy systems. These findings offer a data-driven selection framework for manufacturers looking to localize wind technology in South Asian low-wind-speed corridors.

Keywords: *S-series airfoils; CFD; ANSYS Fluent; ANSYS CFX; wind turbine; aerodynamic performance; lift coefficient; drag coefficient; angle of attack; Pakistan wind energy.*

1. Introduction

Wind energy is one of the fastest-growing renewable energy sources globally, driven by escalating concerns over fossil fuel depletion, rising energy costs, and the imperative to reduce greenhouse gas emissions. Global cumulative installed wind power capacity grew from below 25,000 MW in 2001 to over 700,000 MW by 2020, reflecting annual compound growth rates in the double digits for both wind and solar technologies [1]. In developing nations such as Pakistan, the transition toward renewable energy is particularly urgent. Pakistan's energy demand continues to rise while the country remains heavily dependent on imported fossil fuels, placing considerable strain on the national economy and electrical grid.

Pakistan possesses substantial renewable energy potential, particularly in wind energy. The coastal belt of Sindh and Balochistan — spanning approximately 1,000 km — has an estimated wind energy potential exceeding 346,000 MW [3]. However, only a fraction of this potential (approximately 792 MW) had been harnessed as of recent assessments, largely owing to challenges in site-specific turbine optimization and the lack of tailored aerodynamic technology. The coastal regions of Pakistan experience average wind speeds of 5 to 7 m/s at hub height, corresponding to low Reynolds number flow regimes where conventional airfoil families may not perform optimally.

Airfoils are the fundamental aerodynamic elements of wind turbine blades. Their geometric profile directly governs the lift and drags forces acting on the blade, and consequently, the overall power coefficient (Cp) of the turbine. The National Renewable Energy Laboratory (NREL) developed the S-series family of airfoils specifically for low-speed, low-Reynolds-number wind turbine applications. Among these, the S818, S825, S826, and S828 profiles are designed for inboard to outboard blade regions of horizontal-axis wind turbines (HAWTs) and share geometric similarity that makes them suitable for comparative evaluation.

Despite the growing body of literature on S-series airfoil aerodynamics, a systematic side-by-side comparison of S818, S825, S826, and S828 under identical low-speed CFD conditions, with an explicit focus on the Pakistani wind profile, remains absent. Prior studies have examined individual profiles or partial subsets using various numerical tools, but consistent conditions across all four airfoils — especially including 3D cascade effects and turbulent kinetic energy analysis — have not been reported [8, 12, 18]. This study addresses that gap through a combined 2D and 3D CFD approach, providing comparative aerodynamic data that can directly inform blade design decisions for Pakistan's wind energy sector.

The aerodynamic optimization of wind turbine airfoils at low Reynolds numbers has attracted increasing research attention. Kaya et al. [20] compared NACA, FX, and S-series airfoils at Reynolds numbers ranging from 2×10^5 to 2×10^6, finding that S-series profiles demonstrated clear advantages in delayed stall characteristics and aerodynamic efficiency, particularly at higher angles of attack. At Re = 1×10^6 and 12° AOA, the NACA 6409, FX 60-157, and S4110 airfoils each produced lift coefficients exceeding 1.5, with S4110 achieving a notably high lift-to-drag ratio at 6° AOA.

Jaffar et al. [8] conducted a detailed CFD study of four thick S-series airfoils (S809, S811, S814, and S818) at Re = 1×10^6 and angles of attack from 0° to 20°, employing the k-ω SST turbulence model in ANSYS Fluent. Their results indicated that S811 and S818 outperformed S809 and S814 in the 10°–16° AOA range, exhibiting higher lift, lower drag, and reduced near-wake turbulent kinetic energy. The authors highlighted mid-span HAWT blade sections as particularly suitable for these thicker profiles due to their structural advantages.

Koyuncuoğlu et al. [12] compared S826 and S809 under low Reynolds number conditions using both RANS and URANS solvers with the k-ω SST model. The S826 demonstrated strong agreement with experimental data even in the stall regime, and a 3D unsteady simulation of the same airfoil validated the overall CFD methodology. Their study underscored the importance of resolving laminar-turbulent transition effects, particularly for low-Re wind turbine blade simulations.

The experimental and numerical characterization of S814 and S825 at moderate Reynolds numbers (45,000–90,000) by Hassanzadeh et al. [18] revealed significant performance sensitivity to Reynolds number. The S825 demonstrated stable behavior at medium to high Re values and showed promise for outboard blade sections, while S814 exhibited abrupt lift loss at low Re, indicating premature stall. These findings underscore the relevance of testing S-series profiles specifically within the velocity ranges characteristic of Pakistan's coastal wind resources.

Aloukili et al. [22] applied Co-Flow Jet (CFJ) technology to S818, S825, and S826 airfoils, demonstrating that active flow control could raise lift by up to 109% and lift-to-drag ratio by 146% for S818 at a momentum coefficient of 0.08. This establishes a future pathway for performance enhancement of S-series profiles while simultaneously affirming their baseline aerodynamic characteristics as worthy of further passive optimization study.

Further supporting the rationale for this study, Abbas et al. [6] analyzed wind speed distributions at six Pakistani coastal cities using fourteen probability distribution functions, finding that typical wind speeds at 50 m hub height range from 4.9 to 6.3 m/s — squarely within the 5–10 m/s range examined in the present work. These findings strongly motivate the selection of S-series airfoils for Pakistani wind turbine applications.

2. Methodology

2.1 Airfoil Selection:

Selected airfoils include low Reynolds number profiles, particularly from the S-series, due to their suitability for wind turbine applications in low wind speed regions.

2.2 Computational Domain:

A two-dimensional computational domain was created around each airfoil to simulate airflow behavior. The domain size was chosen sufficiently large to avoid boundary effects.

2.3 Boundary Conditions:

Inlet: Uniform velocity corresponding to desired Reynolds number

Outlet: Pressure outlet condition
Airfoil Surface: No-slip wall condition
Far-field boundaries: Symmetry or free-stream conditions

2.4 Mesh Generation:

A structured mesh with refinement near the airfoil surface was generated to accurately capture boundary layer effects. Grid independence analysis was performed to ensure solution accuracy.

2.5 Governing Equations

The flow was modeled using the incompressible Navier–Stokes Eq. (1) and (2):

Continuity:

$$\nabla \cdot \mathbf{V} = 0 \tag{1}$$

Momentum:

$$\rho(\mathbf{V} \cdot \nabla)\mathbf{V} = -\nabla P + \mu \nabla^2 \mathbf{V} \tag{2}$$

2.6 Turbulence Model

The k–ω SST turbulence model was employed due to its effectiveness in predicting flow separation and adverse pressure gradients, particularly at higher angles of attack.

2.7 Simulation Parameters

Reynolds number range: (insert your actual values)
Angle of attack: (e.g., 0°–20°)
Solver: Pressure-based steady solver
Convergence criteria: Residuals < 10^{-6}

2.8 Performance Metrics

Lift coefficient (Cl)
Drag coefficient (Cd)
Lift-to-drag ratio (Cl/Cd)

2.9 Material and Methods

2.9.1 Airfoil Selection

Four S-series airfoils (S818, S825, S826, and S828) were chosen owing to their effectiveness in low-Reynolds-number wind turbine applications. These airfoils are well suited to low-speed aerodynamic conditions and offer useful characteristics for comparative performance analysis. As shown in Figure 1, the selected profiles differ in their camber and thickness distributions, which play an important role in determining pressure distribution, lift development, and drag characteristics.

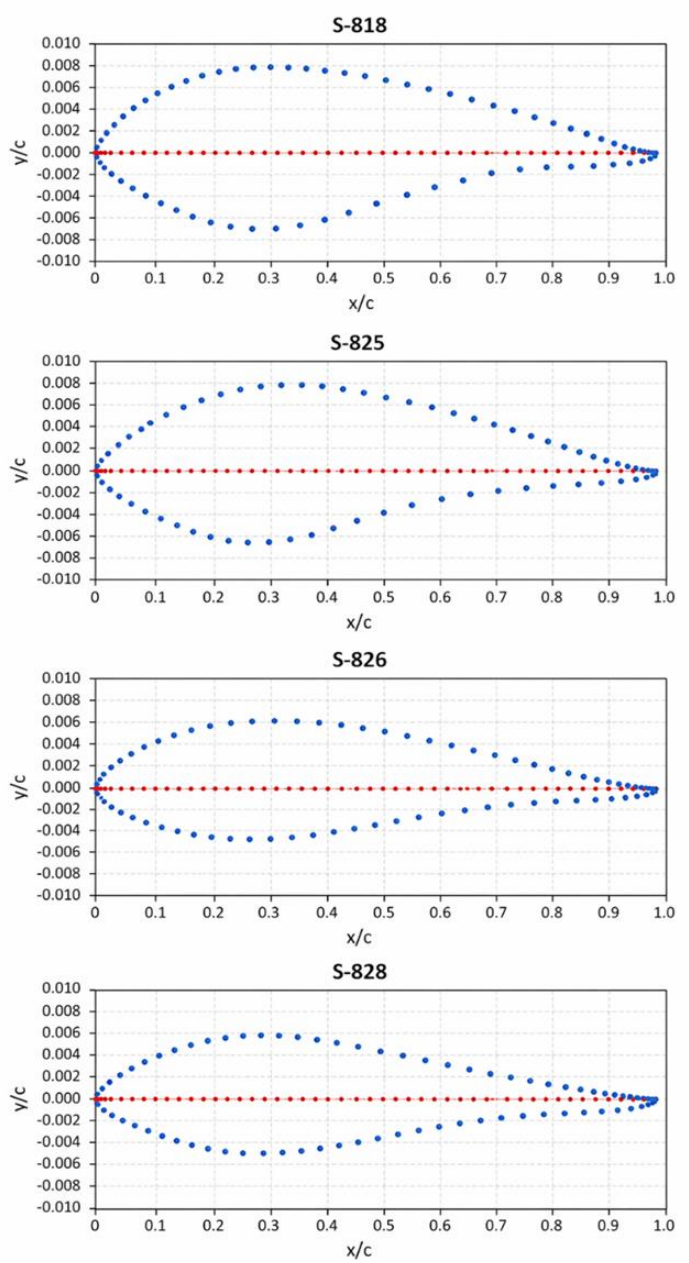

Figure 1 Geometric profiles of selected S-series airfoils (S818, S825, S826, and S828)

Therefore, the chosen airfoils provide a suitable foundation for evaluating aerodynamic behavior under the specified operating conditions.

2.9.2 Geometry Modeling

The airfoil coordinates were obtained from standard databases and modeled as two-dimensional profiles as shown in Figure 2. The chord length was normalized to unity to maintain consistency in comparative analysis.

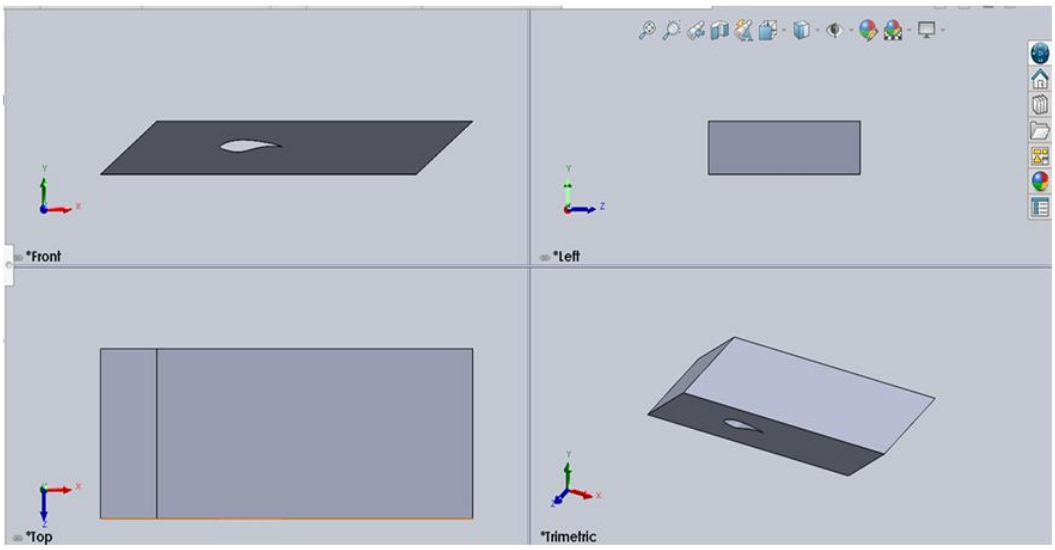

Figure 2 CAD model of the airfoil geometry in different views

2.9.3 Computational Domain

A 2D computational domain was created around each airfoil with sufficient upstream and downstream distances to minimize boundary effects and accurately capture wake behavior.

2.9.4 Mesh Generation

A structured mesh with boundary layer refinement was generated. Inflation layers were applied near the airfoil surface to resolve near-wall flow. A grid independent study was conducted to ensure accuracy of results.

2.9.5 Simulation Setup

The numerical simulations were carried out in ANSYS Fluent under steady-state and incompressible flow conditions using a pressure-based solver. This setup was selected to ensure reliable prediction of the aerodynamic behavior of the selected airfoils under low-speed operating conditions. The adopted assumptions are appropriate for analyzing external flow characteristics such as pressure distribution, velocity contours, and wake formation around the airfoil. A representative simulation result for the S818 airfoil at an angle of attack of 5° and a flow velocity of 10 m/s is presented in Figure 3, which illustrates the velocity contour around the airfoil and highlights the acceleration of flow over the upper surface along with the downstream wake region. Similarly, the remaining selected airfoils were analyzed under the same simulation setup and boundary conditions to ensure a consistent and reliable comparative aerodynamic assessment.

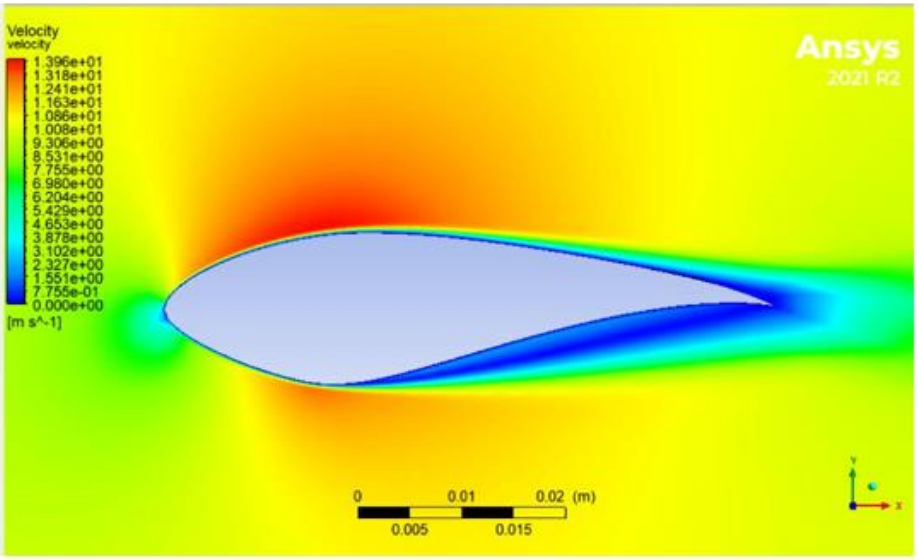

Figure 3 S818 5 degree at velocity 10

2.9.6 Boundary Conditions

Inlet: Uniform velocity
Outlet: Pressure outlet
Airfoil: No-slip wall
Far-field: Symmetry condition

2.9.7 Turbulence Model

The **k–ω SST turbulence model** was used due to its accuracy in predicting flow separation and near-wall effects.

2.9.8 Performance Parameters

Lift coefficient (Cl)
Drag coefficient (Cd)
Lift-to-drag ratio (Cl/Cd)
Pressure distribution
Velocity distribution
Turbulent kinetic energy (TKE)

2.9.9 Post-Processing

Results were analyzed using plots of:

Pressure vs chord length
Velocity vs chord length
TKE vs chord length
Cl and Cd vs angle of attack

3. Results and Discussion

3.1 Pressure Distribution

Pressure distribution along the chord shows a significant pressure difference between upper and lower surfaces, indicating effective lift generation. Airfoils with higher camber exhibited stronger pressure gradients.

3.2 Velocity Distribution

Velocity contours reveal acceleration over the upper surface and deceleration near the lower surface. Flow separation was observed at higher angles of attack.

3.3 Turbulent Kinetic Energy

TKE analysis indicates variations in turbulence intensity across different airfoils. Lower TKE values correspond to reduced wake losses and improved aerodynamic efficiency where Figure 4 shows that the S818 airfoil exhibits a pronounced peak in turbulent kinetic energy near the forward portion of the chord, followed by a rapid decline toward the mid-chord region. This behavior indicates strong turbulence generation near the leading edge, likely caused by rapid acceleration of the flow and early boundary-layer disturbances.

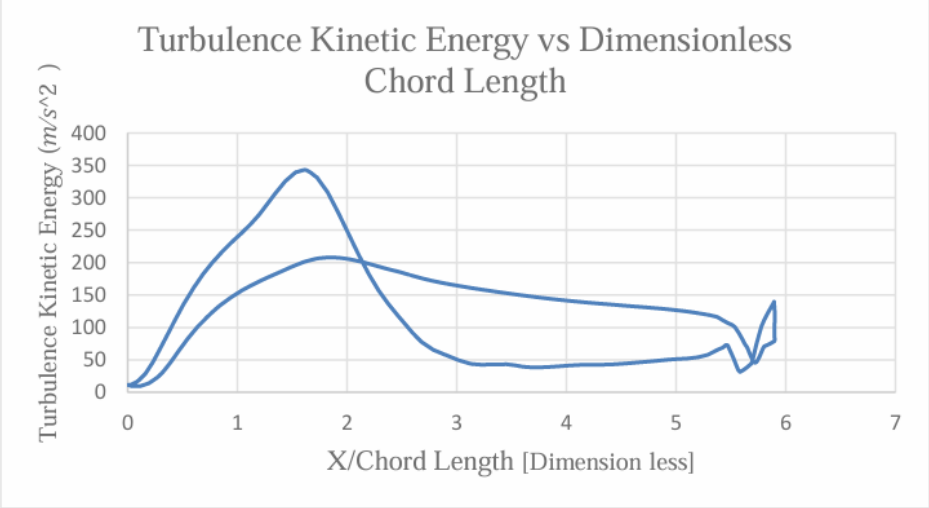

Figure 4 S818

After the initial peak, the turbulence level decreases considerably, suggesting partial stabilization of the flow over the middle chord. However, a small rise is again visible near the trailing-edge

region, which may be associated with wake formation and localized flow instability. Overall, S818 demonstrates relatively strong turbulence production near the front portion of the airfoil, indicating higher local aerodynamic activity and potentially greater viscous losses than the smoother profiles.

TKE distribution for S825 Figure 5 indicates that the S825 airfoil has a comparatively moderate turbulent kinetic energy distribution. The TKE rises from the leading edge and reaches a peak earlier in the chord, but the maximum value is lower than that observed for S818. After the peak, the curve declines and remains at moderate levels over much of the chord length, suggesting a more controlled turbulence development. A slight increase near the trailing edge is again present, reflecting wake effects. Compared with S818, the S825 profile appears to maintain a more balanced turbulence structure, which may contribute to improved aerodynamic stability and reduced energy dissipation.

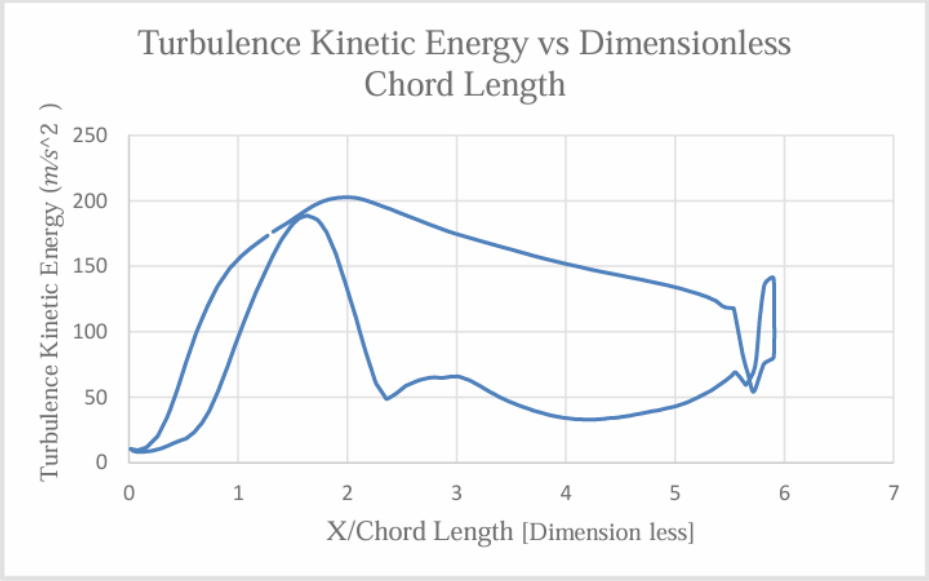

Figure 5 S825

TKE distribution for S826 Figure 6 shows that the S826 airfoil also exhibits a moderate TKE peak in the front region, followed by a noticeable reduction across the mid-chord section. The turbulence level remains relatively low over a considerable portion of the chord, indicating that the flow over this airfoil becomes more stable after the initial leading-edge disturbances. Near the trailing edge, the curve increases slightly, which is typical of wake-induced turbulence. In comparison with S818, the S826 profile appears to generate less intense turbulent fluctuations overall, suggesting comparatively smoother aerodynamic performance and potentially lower wake losses.

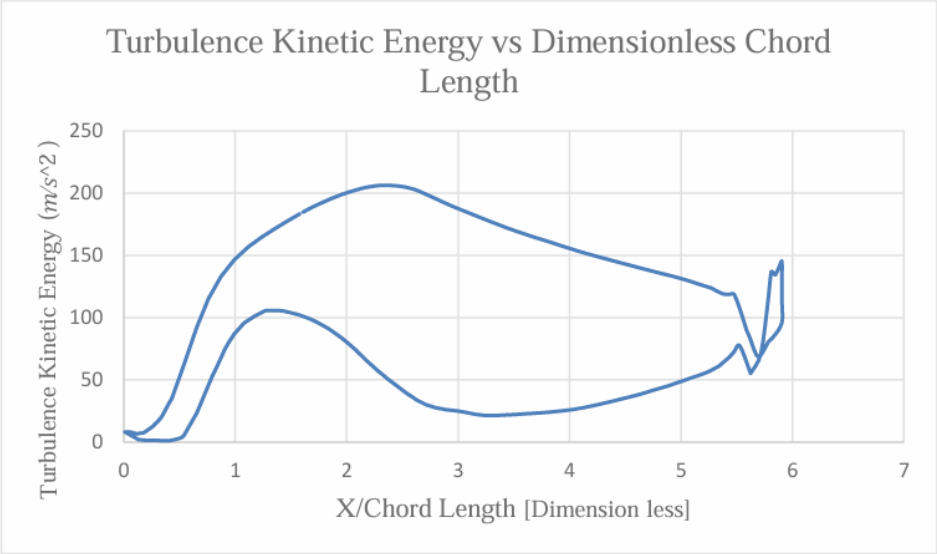

Figure 6 S826

TKE distribution for S828 Figure 7 presents the TKE behavior for the S828 airfoil. This profile exhibits a broader and smoother turbulence distribution, with the peak shifted farther downstream compared with the other airfoils. Instead of a sharp spike, the TKE grows gradually and remains relatively sustained over a larger portion of the chord.

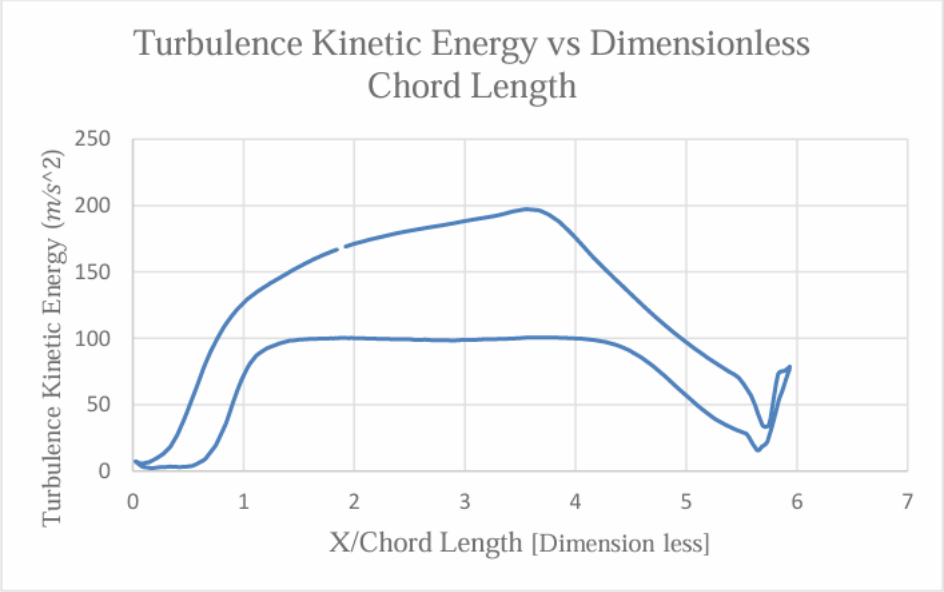

Figure 7 S828

Further, this suggests that turbulence develops in a more distributed manner, rather than being concentrated at a single region. Such behavior is often associated with smoother energy transfer in the boundary layer and better flow management over the surface. Although a reduction is observed near the trailing-edge region, the overall trend indicates that S828 provides comparatively stable aerodynamic characteristics with less abrupt turbulence fluctuations. Velocity distribution for S818 Figure 8 shows that the S818 airfoil experiences a sharp increase in velocity near the leading edge, reaching a high peak before decreasing significantly along the downstream direction. This trend indicates strong flow acceleration over the upper surface, which is beneficial for lift generation, but the rapid drop afterward suggests the presence of a strong adverse pressure gradient. The near-zero velocity region over part of the chord implies possible boundary-layer thickening or flow separation. Toward the trailing edge, the velocity rises again slightly, indicating wake adjustment. Thus, S818 generates strong suction effects but may also be more prone to separation and associated aerodynamic losses.

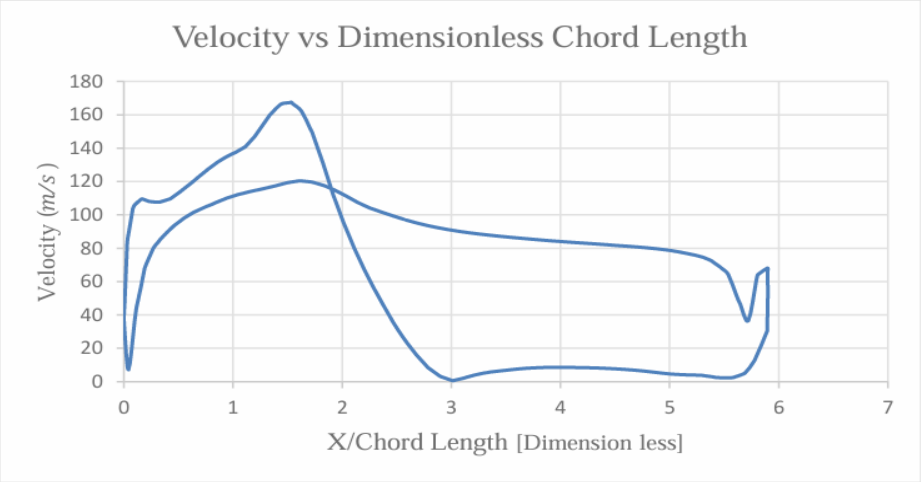

Figure 8 S818

Velocity distribution for S825 Figure 9 reveals that the S825 airfoil has a more gradual velocity increase from the leading edge, followed by a smoother decline across the chord. Compared with S818, the maximum velocity is slightly lower, but the profile appears more stable and less abrupt. This suggests a more favorable pressure recovery and reduced tendency for early flow separation. The lower-surface velocity behavior also remains comparatively smoother, indicating balanced flow development around the airfoil. Overall, S825 demonstrates more controlled aerodynamic behavior and likely better flow attachment over a larger portion of the surface.

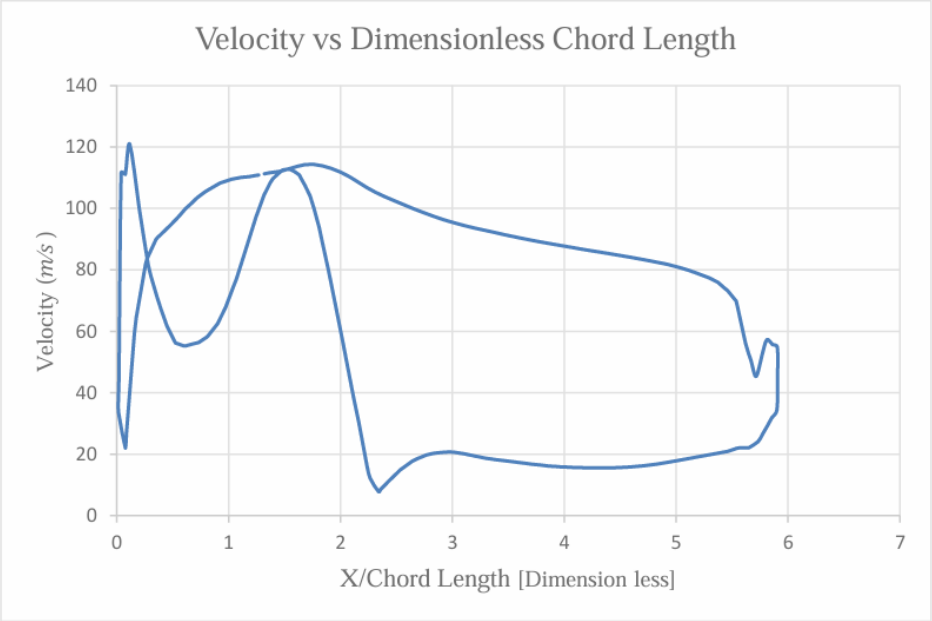

Figure 9 S825

Velocity distribution for S826 Figure 10 shows that the S826 airfoil follows a similar pattern to S825, with an increase in velocity near the leading edge and a progressive decline toward the trailing edge.

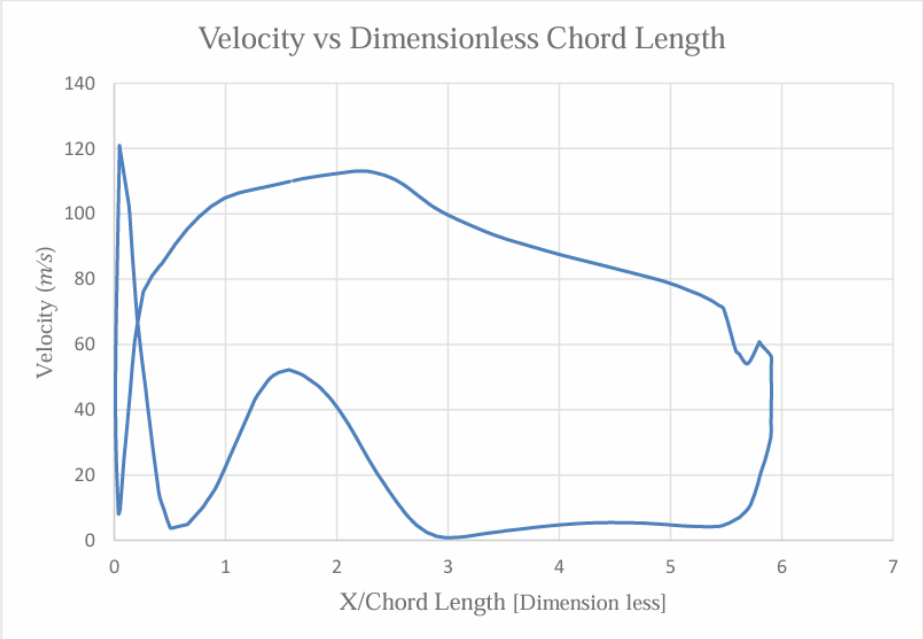

Figure 10 S826

However, the reduction in velocity on one branch of the curve is more pronounced, indicating a stronger deceleration region and a possible local separation tendency. Even so, the overall variation remains smoother than that of S818. This suggests that S826 offers a compromise between strong acceleration and acceptable flow stability, though its separation characteristics may be slightly less favorable than S825 under the same conditions.

Velocity distribution for S828 Figure 11 demonstrates that the S828 airfoil has the smoothest and most sustained velocity profile among the airfoils considered.

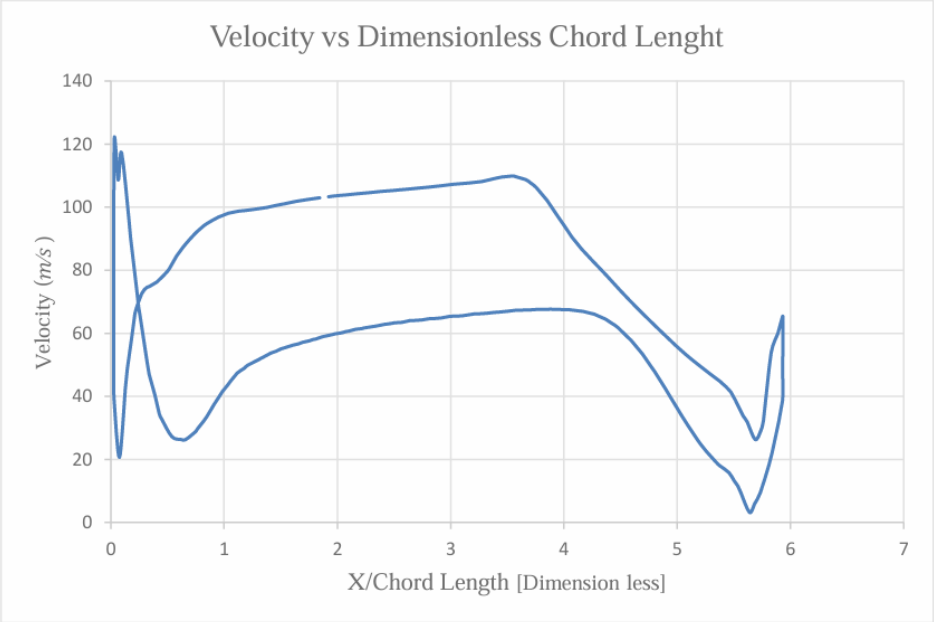

Figure 11 S828

After the initial leading-edge acceleration, the velocity remains relatively elevated over a long portion of the chord before gradually decreasing. This indicates prolonged attached flow and a more stable boundary-layer development. The smoother recovery toward the trailing edge suggests reduced severity of adverse pressure gradients and improved aerodynamic efficiency. Compared with the other airfoils, S828 appears to provide the most stable flow structure, which is consistent with its broader and smoother TKE behavior.

3.4 Aerodynamic Performance

The aerodynamic performance of the selected S-series airfoils was evaluated through pressure distribution, lift coefficient, drag coefficient, and lift-to-drag ratio at flow velocities of 5 m/s and 10 m/s. The results provide a comparative understanding of how the airfoil geometry influences flow behavior, loading characteristics, and overall aerodynamic efficiency. Lift coefficient increases with angle of attack until stall, Drag increases gradually and sharply post-stall, S-series airfoils show improved Cl/Cd ratios. Pressure distribution on S818 Figure 12 shows that the S818

airfoil develops a strong pressure variation along the chord. A very high pressure is observed near the leading-edge stagnation region, followed by a sharp pressure drop over one surface, indicating strong local acceleration of the flow. The minimum pressure occurs around the forward chord region, after which a gradual recovery is observed toward the trailing edge. This large pressure difference between the upper and lower surfaces confirms lift generation.

However, the relatively steep pressure gradient suggests that S818 may experience stronger adverse pressure recovery, which can increase the tendency for boundary-layer instability and early separation compared with smoother profiles.

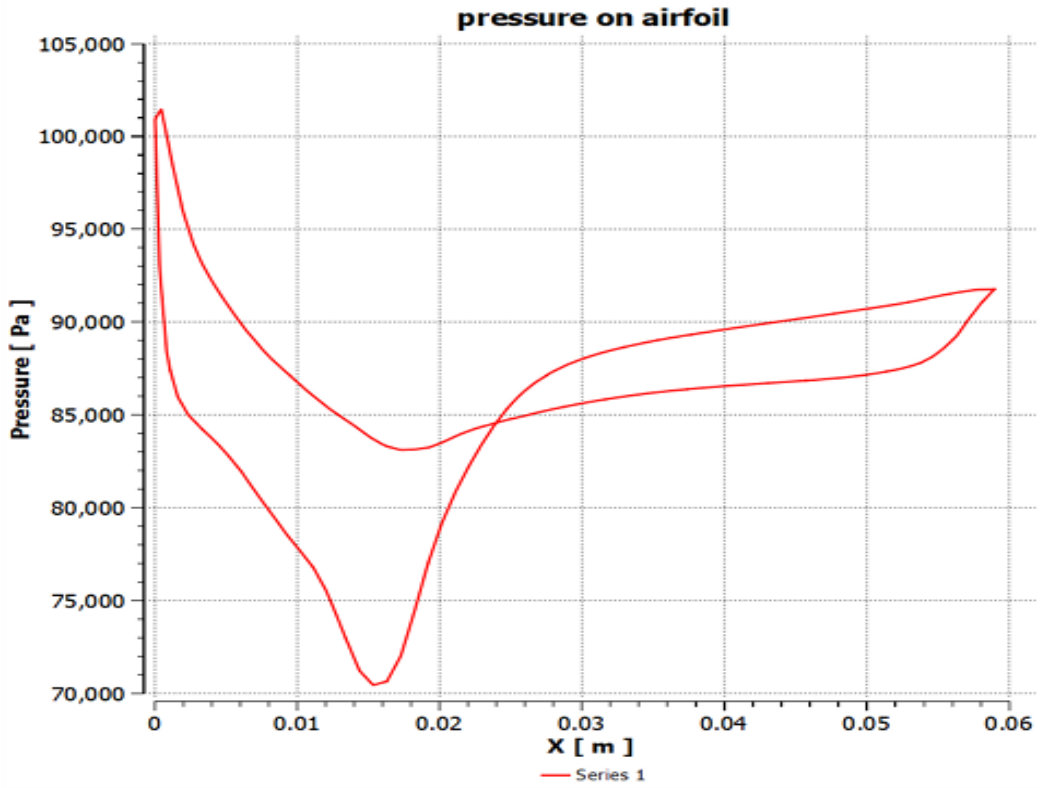

Figure 12 S818

The Pressure distribution on S825 as shown in Figure 13 which indicates that the S825 airfoil exhibits a smoother pressure variation than S818. Although the pressure difference between the two surfaces remains significant enough to generate lift, the pressure recovery is more gradual. The suction peak is still visible near the front portion of the airfoil, but the overall distribution is less abrupt. This behavior suggests a more controlled acceleration-deceleration process over the chord, which is beneficial for maintaining attached flow and reducing aerodynamic penalties associated with strong adverse pressure gradients.

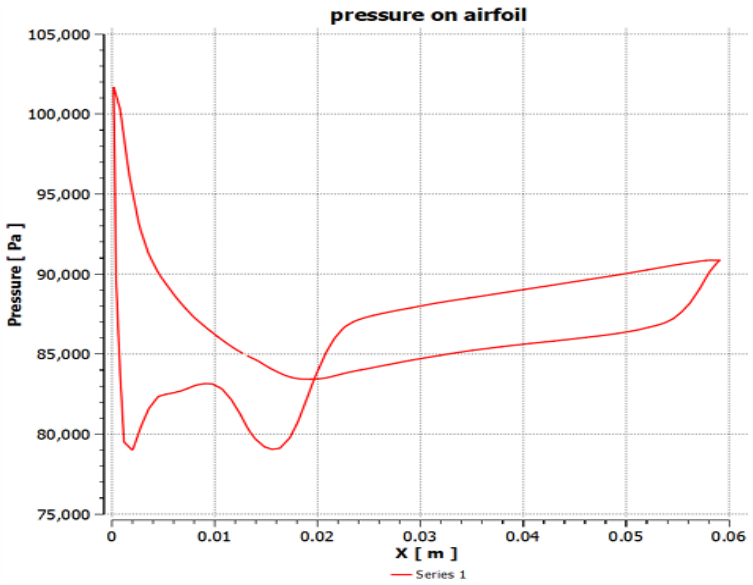

Figure 13. S825

Pressure distribution on S826 Figure 14 shows that the S826 airfoil produces a comparatively balanced pressure distribution. The separation between the two pressure curves is clear, indicating effective lift generation, while the pressure recovery appears smoother than in S818 and comparable to or slightly better than S825. The reduced abruptness in the pressure change suggests improved flow stability over the airfoil surface. This behavior is consistent with an airfoil that can sustain favorable aerodynamic loading without severe flow disturbances over much of the chord.

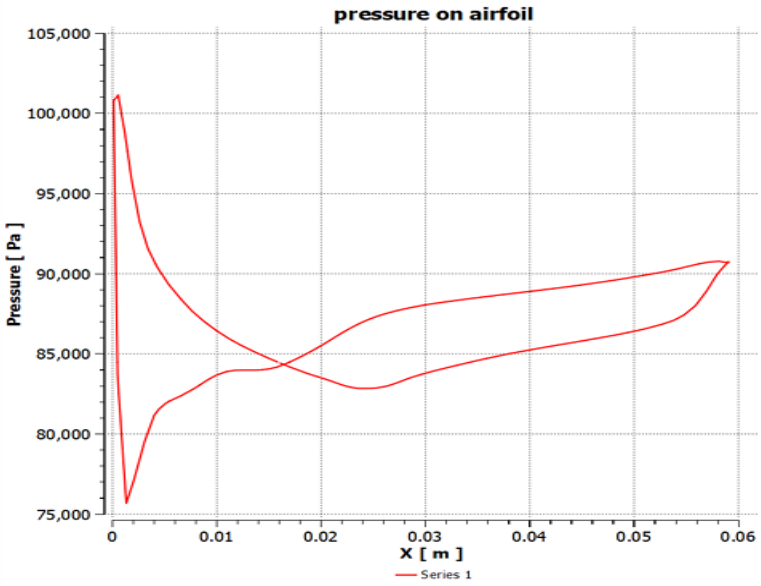

Figure 14 S826

Pressure distribution on S828 as shown in Figure 15 which presents the pressure distribution for S828, which appears among the smoothest of the four airfoils. The pressure variation along the chord is more uniform, and the recovery toward the trailing edge is gradual. This indicates a comparatively stable boundary-layer development and a reduced likelihood of strong localized separation. Although the peak suction is not the most aggressive among the airfoils, the smoother pressure behavior implies better aerodynamic refinement and a more efficient distribution of loading over the chord.

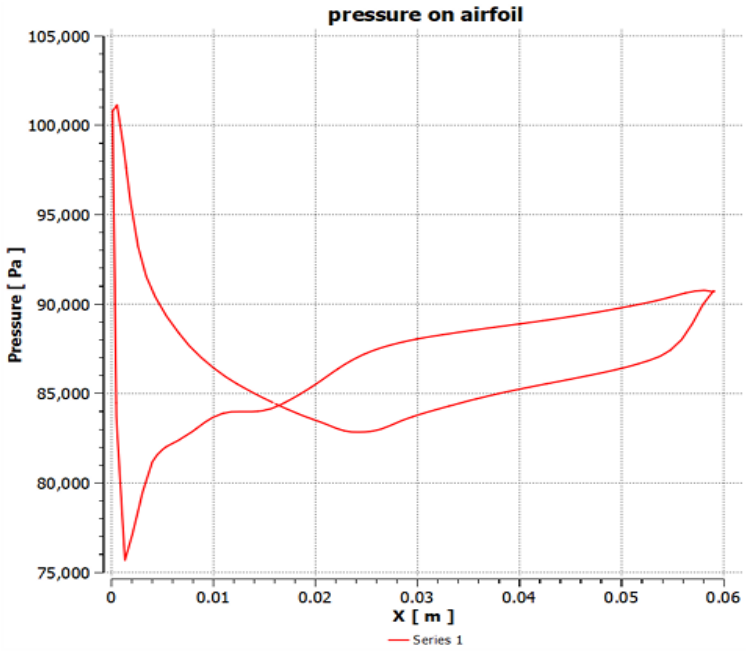

Figure 15 S828

Lift Coefficient Results at different angles of attack at 5 m/s and 10 m/s are illustrated, where Coefficient of lift vs angle of attack at 5 m/s as shown in Figure 16 states that, at 5 m/s, the lift coefficient generally increases with angle of attack for all airfoils, although the rate of increase differs significantly. S825 exhibits the strongest lift growth and reaches the highest C_l values at larger angles of attack, indicating superior lift-generating capability under this condition. S826 also performs strongly, with a steady increase and relatively high lift values, though slightly below S825 at the upper end of the range. S828 shows moderate lift growth, while S818 demonstrates the weakest improvement, remaining at relatively low lift values throughout. These results indicate that, at low flow speed, S825 and S826 are more effective in converting angle-of-attack increase into useful aerodynamic lift.

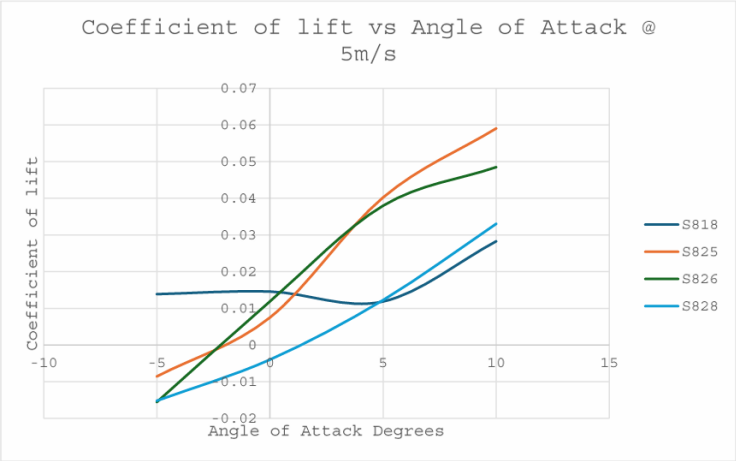

Figure 16 Comparison of lift coefficient (C_l) versus angle of attack for S818, S825, S826, and S828 airfoils at 5 m/s.

Figure 17 illustrates the variation of drag coefficient (Cd) with angle of attack for the S818, S825, S826, and S828 airfoils at a flow velocity of 5 m/s. The results indicate that the drag coefficient initially decreases slightly at lower angles of attack and then rises as the angle of attack increases further. Among the selected airfoils, S828 exhibits the lowest drag values over most of the operating range, indicating comparatively better aerodynamic efficiency under low-speed conditions. In contrast, S818 shows the highest drag values, suggesting greater flow resistance. The drag behavior of S825 and S826 remains intermediate, with both airfoils showing a sharper drag increase at higher angles of attack. This trend confirms that increasing incidence increases aerodynamic losses, especially near the upper operating range.

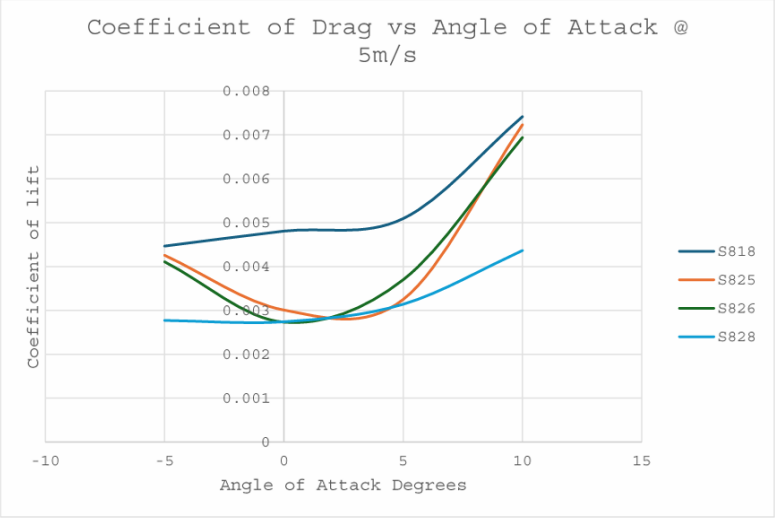

Figure 17 Comparison of drag coefficient (C_d) versus angle of attack for S818, S825, S826, and S828 airfoils at 5 m/s.

Figure 18 presents the variation of lift coefficient (Cl) with angle of attack for the selected airfoils at a flow velocity of 10 m/s. It is evident that the lift coefficient generally increases with angle of attack for all airfoils, although the rate of increase differs significantly. Among the four profiles, S826 demonstrates the strongest lift growth and achieves the highest Cl values at larger angles of attack, indicating superior lift-generating capability at this velocity. S825 also shows a steady and favorable increase in lift, though its performance remains below that of S826 at higher incidence. In comparison, S818 and S828 exhibit relatively moderate lift development. Thus, as shown in Figure 18, S826 provides the most effective lifting performance at 10 m/s.

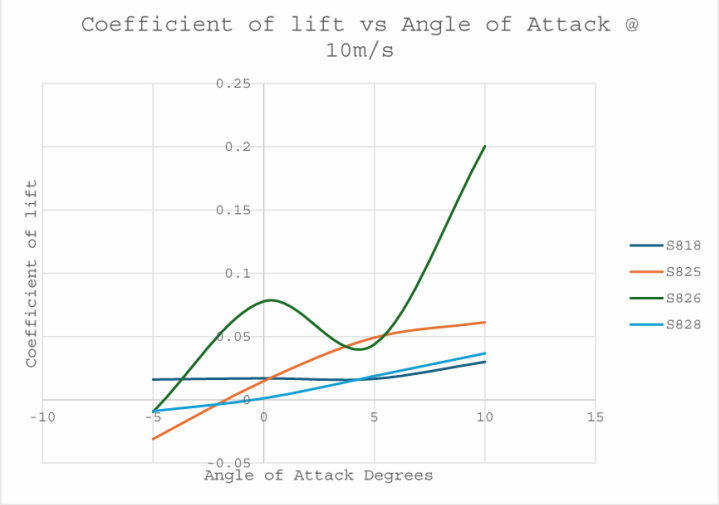

Figure 18 Comparison of lift coefficient (C_l) versus angle of attack for S818, S825, S826, and S828 airfoils at 10 m/s.

Figure 19 shows the variation of drag coefficient (Cd) with angle of attack for the S-series airfoils at 10 m/s. The results reveal that drag increases with increasing angle of attack, but the extent of this increase differs among the airfoils. S826 experiences a pronounced rise in drag at larger angles of attack, which is consistent with its strong lift generation and may indicate increased pressure drag and possible onset of flow separation. S825 shows relatively high drag at negative angle of attack, followed by lower drag in the moderate operating region and then a gradual increase. S818 maintains a comparatively moderate drag trend, whereas S828 again exhibits the lowest drag values throughout most of the range. Therefore, Figure 19 suggests that S828 remains the most drag-efficient profile even at the higher flow velocity.

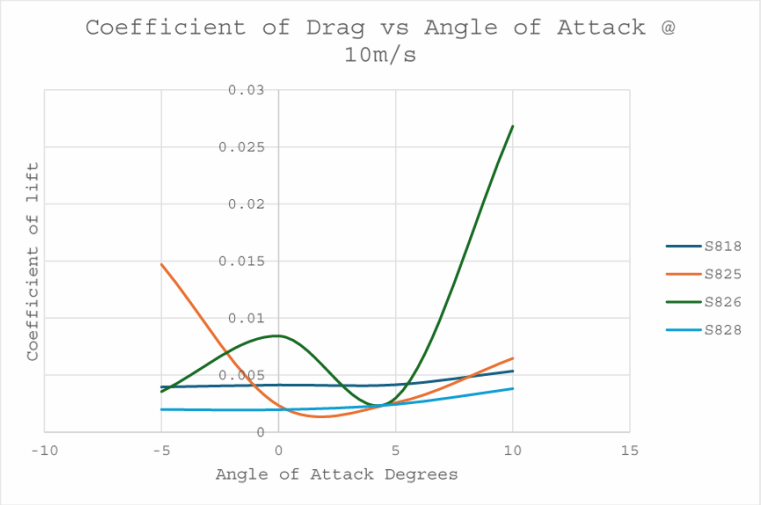

Figure 19 Comparison of drag coefficient (C_d) versus angle of attack for S818, S825, S826, and S828 airfoils at 10 m/s.

Figure 20 compares the lift-to-drag ratio (Cl/Cd) versus angle of attack at 10 m/s. This figure provides an overall measure of aerodynamic efficiency by combining both lift and drag characteristics. The results show that S825 achieves the highest peak Cl/Cd value, indicating the best overall aerodynamic efficiency at moderate angles of attack. S826 also performs strongly, with a high lift-to-drag ratio over a wide operating range, although its peak remains slightly below that of S825. S828 shows a gradual improvement in efficiency with increasing angle of attack, while S818 records the lowest Cl/Cd values overall. Hence, as illustrated in Figure 20, S825 offers the best compromise between lift generation and drag penalty at 10 m/s.

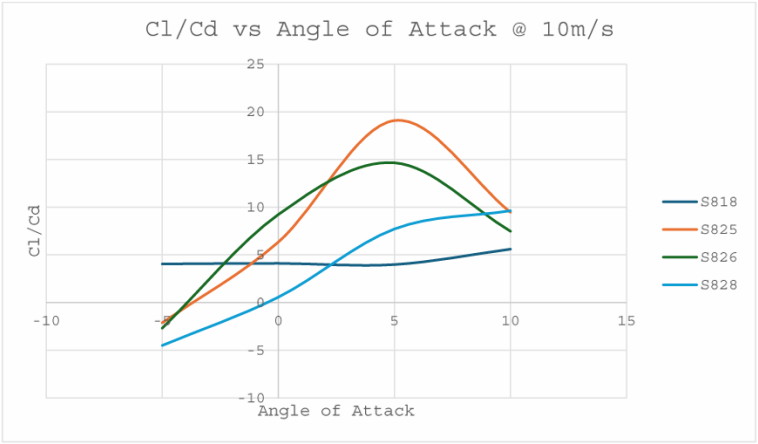

Figure 20 Comparison of lift-to-drag ratio (C_l/C_d) versus angle of attack for S818, S825, S826, and S828 airfoils at 10 m/s.

Figure 21 illustrates the variation of lift-to-drag ratio (Cl/Cd) with angle of attack at 5 m/s. The results indicate that S826 attains the highest peak aerodynamic efficiency at low speed, followed closely by S828. This shows that both airfoils are particularly suitable for low-Reynolds-number operation where efficient lift production with limited drag is required. S825 demonstrates moderate performance, while S818 remains the least efficient among the four profiles. The comparatively strong performance of S826 at 5 m/s suggests that it combines high lift capability with acceptable drag characteristics, whereas S828 benefits mainly from its consistently low drag values. Thus, Figure 21 confirms that S826 and S828 are the most efficient airfoils under low-speed conditions.

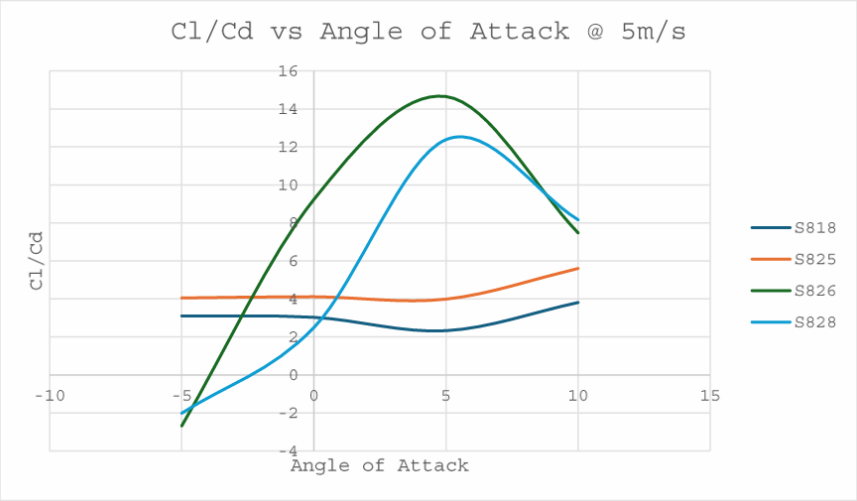

Figure 21 Comparison of lift-to-drag ratio (C_l/C_d) versus angle of attack for S818, S825, S826, and S828 airfoils at 5 m/s.

3.6 Overall Comparative Discussion

A comparison of all results shows that the aerodynamic response of the selected S-series airfoils varies considerably with both airfoil geometry and operating velocity. S818 exhibits stronger local pressure gradients, higher turbulence intensity, and relatively high drag, making it less efficient overall despite its ability to generate lift. S825 provides strong lift performance at 5 m/s and achieves the highest lift-to-drag ratio at 10 m/s, indicating excellent aerodynamic balance at moderate-to-higher flow speed. S826 demonstrates the strongest lift generation, particularly at 10 m/s, and also attains the highest aerodynamic efficiency at 5 m/s, making it highly effective under low-speed wind turbine operating conditions. S828, although not producing the highest lift, consistently shows the smoothest velocity and pressure distributions together with the lowest drag, indicating stable flow behavior and good aerodynamic refinement. Overall, the results suggest that S825 and S826 are the most competitive airfoils for aerodynamic performance, while S828 stands out for its low-drag and stable-flow characteristics. In contrast, S818 appears comparatively less efficient due to stronger turbulence generation, steeper pressure gradients, and higher drag levels. These findings confirm that the suitability of an airfoil depends not only on its lift capability but also on its drag characteristics, boundary-layer stability, and operating Reynolds number.

4. Conclusion

This study numerically evaluated the aerodynamic performance of the S818, S825, S826, and S828 airfoils under low-speed wind conditions using CFD simulations, and the results demonstrated that aerodynamic efficiency is strongly governed by both airfoil geometry and operating conditions. Comparative assessment of pressure distribution, velocity contours, turbulent kinetic energy, lift coefficient, drag coefficient, and lift-to-drag ratio showed clear differences among the selected profiles, with S828 exhibiting the most stable and efficient aerodynamic behavior due to its smoother pressure recovery, lower drag, and delayed flow separation, while S825 also showed strong overall performance with a favorable lift-to-drag ratio. S826 displayed excellent lift-generating capability, particularly at higher flow velocity, whereas S818 showed comparatively lower aerodynamic efficiency because of stronger turbulence effects and higher drag penalties. In general, the most favorable aerodynamic performance was observed at moderate angles of attack, while further increase in angle of attack led to performance deterioration associated with stall onset. Although the present study provides useful insight into the comparative aerodynamic characteristics of these airfoils, it is limited to numerical simulations under steady low-speed conditions and does not include experimental validation, three-dimensional blade effects, surface roughness, structural interaction, or unsteady atmospheric inflow conditions that may influence actual wind turbine performance. Therefore, future work should focus on experimental verification of the numerical findings, extension to three-dimensional rotating blade analysis, investigation under a wider range of Reynolds numbers and turbulence conditions, and optimization of airfoil geometry for improved performance in practical low-Reynolds-number wind energy applications.

References

[1] Dincer, F. (2011). The analysis on wind energy electricity generation status, potential and policies in the world. Renewable and Sustainable Energy Reviews, 15(9), 5135–5142.

[2] Eriksson, S., Bernhoff, H., & Leijon, M. (2006). Evaluation of different turbine concepts for wind power. Renewable and Sustainable Energy Reviews.

[3] Irfan, M., Zhang, Z.-Y., Mukeshimana, M. C., & Ahmad, M. (2019). Wind energy development in South Asia: Status, potential and policies.

[4] Gray, A., Singh, B., & Singh, S. (2021). Low wind speed airfoil design for horizontal axis wind turbine.

[5] Yi, M., Jianjun, Q., & Yan, L. (2015). Airfoil design for vertical axis wind turbine operating at variable tip speed ratios.

[6] Abbas, G., et al. (2025). Advancing wind energy potential estimation through multi-distribution wind speed analysis in coastal Pakistan.

[7] Lu, H., et al. (2021). On airfoil research and development: History, current status, and future directions.

[8] Jaffar, H. M., Al-Salihi, L. A., & Khalil, A. A. (2023). Aerodynamic characteristics evaluation of S-series airfoils.

[9] Kassa, B. Y., et al. (2024). Aerodynamic performance characteristics of low Re airfoils: A parametric and multi-criteria decision study.

[10] Wang, L., et al. (2024). A review of intelligent airfoil aerodynamic optimization methods based on data-driven advanced models.

[11] Nhung, L. T. T., et al. (2024). CFD analysis of key factors impacting the aerodynamic performance of the S830 wind turbine airfoil.

[12] Yilmaz, O. (2018). Numerical investigation of aerodynamic characteristics of low Reynolds number airfoils S826 and S809.

[13] Corte Real, E., et al. (2020). An assessment of different turbulence models on a CFD simulation of airflow past an S814 airfoil.

[14] Uddin, S. M. N., et al. (2023). Numerical investigation of the enhancement of the aerodynamic performance for newly modified blended airfoils utilizing S809, S829, and NACA 2412 baseline shapes.

[15] Supreeth, R., et al. (2019). Experimental and numerical investigation of the influence of leading-edge tubercles on S823 airfoil behavior.

[16] Biedermann, T., & Al-Salihi, L. A. (2023). Aerodynamic characteristics evaluation of S-series airfoils.

[17] El Hady, M. A. (2020). A comparative study for different shapes of airfoils.

[18] Hassanzadeh, A., Hassanzadeh, T., & Naughton, J. W. (2019). Static and dynamic aerodynamic performance of the NREL S814 and S825 airfoils at moderate Reynolds number.

[19] Didane, D. H., et al. (2021). 2D CFD simulation study on the performance of various NACA airfoils.

[20] Kaya, M. N., & Kose, H. (2021). Comparison of aerodynamic performances of various airfoils from different airfoil families using CFD.

[21] Shahrokhi, S. S., et al. (2024). Aerodynamic design of a double slotted morphed flap airfoil — a numerical study.

[22] Aloukili, A. M., et al. (2024). Co-flow jet effects on the aerodynamic performance of NREL aerofoils with different thicknesses for wind turbine applications.

[23] Ahmad, M., & Abid, M. Z. (2023). Airfoil shape impact assessment for improved aerodynamics in hybrid VAWT applications. Power Generation Technology, 1.